Exploring 4D microstructural evolution in a heavily deformed ferritic alloy

Yildirim, Can; Detlefs, Carsten; Zelenika, Albert; Poulsen, Henning F.; Rodriguez-Lamas, Raquel; Cook, Philip K.; Kutsal, Mustafacan; Mavrikakis, Nikolas

Published in:
Journal of Physics: Conference Series

Link to article, DOI:
10.1088/1742-6596/2635/1/012040

Publication date:
2023

Document Version
Publisher's PDF, also known as Version of record

Journal of Physics: Conference Series

Exploring 4D microstructural evolution in a heavily deformed ferritic alloy

Exploring 4D microstructural evolution in a heavily deformed ferritic alloy

Can Yildirim[1], Carsten Detlefs[1], Albert Zelenika[1,2] Henning F. Poulsen[2], Raquel Rodriguez-Lamas[1], Philip K. Cook[1], Mustafacan Kutsal[2] and Nikolas Mavrikakis[3]

[1] European Synchrotron Radiation Facility, 38043 Grenoble, France
[2] Department of Physics, Technical University of Denmark, 2800 Kgs. Lyngby, Denmark
[3] OCAS, Pres. J.F. Kennedylaan 3, BE-9060, Zelzate, Belgium
E-mail: can.yildirim@esrf.fr

Abstract. We present a multi-scale study of recrystallization annealing of an 85% cold rolled Fe-3%Si alloy using a combination of dark field X-ray microscopy (DFXM), synchrotron X-ray diffraction (SXRD), and electron backscatter diffraction (EBSD). The intra-granular structure of the as-deformed grain reveals deformation bands separated by $\approx$ 3–5°misorientation. We monitor the structural evolution of a recrystallized grain embedded in bulk, from the early stages of recrystallization to 65% overall recrystallization through isothermal annealing steps. Results show that the recrystallized grain of interest (GOI) grows much faster than its surroundings yet remains constant in size as the recrystallization proceeds. Isolated dislocations embedded within the volume of the recrystallized GOI are investigated.

1. Introduction

Recrystallization and grain growth are important phenomena that occur in deformed metals during annealing. During the deformation of metals, new defects such as vacancies and dislocations are generated which increase the free energy of a given crystal. The density and distribution of these defects not only determine the hardening in the deformed state, but also constitute the main driving force for annealing phenomena. As physical and material properties depend on the state of the deformed and recrystallized microstructures, understanding the nucleation and growth of recrystallization in deformed materials is of great industrial significance.

The experimental understanding of strengthening mechanisms in the deformed state, and subsequent recrystallization during annealing, has improved drastically over the past 30 years. Notably, with the introduction of electron backscatter diffraction (EBSD) in scanning electron microscopes, fast and automated data collection providing morphological and crystallographic information can be employed. Studies in the last decades have shown that the distribution of the recrystallized (RX) grains is highly influenced by the local deformation microstructure [1, 2]. Both 2D and 3D EBSD methods have been the number one methods of choice of many researchers in assessing the geometrically necessary dislocation (GND) densities in deformed materials over the past years [3–6]. Even though these studies improved our understanding of the static dislocations structures in deformed metals, electron-based techniques have limited possibilities of dynamic studies within bulk material, due to sample preparation requirements.

X-ray based techniques have improved our understanding of the relation between the deformed and the annealed states within the past 20 years. Synchrotron-based techniques such as 3D X-ray diffraction, or High Energy Diffraction Microscopy (3DXRD or HEDM) [7, 8], Diffraction Contrast Tomography (DCT) [9] and Differential Aperture X-ray Microscopy (DAXM) [10] have been used to investigate recrystallization and growth phenomena in 3D and 4D (x, y, z, t). While these studies have provided

fascinating insights on the recrystallization and growth of near perfect grains within bulk materials, they fail to capture the multi-scale relation between the new nuclei and the highly deformed matrix due to limited spatial resolution and the peak overlap problem [11].

A relatively new synchrotron-based method called Dark Field X-ray Microscopy (DFXM) provides an alternative approach to the above-mentioned challenges. DFXM is a diffraction imaging method for probing 3D nanostructures with their associated strain and orientation in bulk materials, with better angular resolution than its electron counterparts [12–14]. The microscope can be coupled with 3DXRD and DCT [15], and quantitative texture analysis can also be performed [16].

Here, we investigate recrystallization and grain growth from a heavily deformed ferritic alloy using DFXM, SXRD and EBSD. We monitor the 4D evolution of a recrystallized grain of interest (GOI) upon successive annealing steps up to RX=65% overall recrystallization using DFXM. We explore the orientation relations between the deformed structure and the new grains during annealing in a bulk and industrially-relevant deformed sample.

2. Experimental

2.1. EBSD

Global recrystallization tendencies were followed with EBSD in the as-deformed condition and after interrupted annealing in a dilatometer at 600 °C. More details about the EBSD measurements can be found in [17].

2.2. DFXM and SXRD

The DFXM experiments were conducted at Beamline ID06-HXM at the European Synchrotron Radiation Facility (ESRF) [18]. We used a monochromatic beam with $17\,\mathrm{keV}$ photon energy. The beam was focused in the vertical direction using a Compound Refractive Lens (CRL) comprised of 58 1D Be lenslets with an R=100 μm radius of curvature, yielding an effective focal length of $72\,\mathrm{cm}$. The beam profile on the sample was approximately $200\times0.6\,\mu\mathrm{m}^2$ (FWHM) in the horizontal and vertical directions, respectively. The horizontal *line beam* illuminated a single plane that sliced through the depth of the crystal, defining the microscope's *observation plane*, as shown in figure 1. For the SXRD experiments a FReLoN CCD 2D detector was used having $47.3\,\mu\mathrm{m}$ pixel size positioned at 170 mm from the sample. This camera was used to measure the texture of the 110 diffraction ring [16], and to locate the high stored energy (HSE) regions for high resolution DFXM measurements. A near-field camera with $0.622\,\mu\mathrm{m}$ pixel size was then placed $56\,\mathrm{mm}$ downstream the sample, and used to orient the crystal into the Bragg condition, to calibrate the temperature on the sample using the lattice parameter expansion, and to measure local orientation after each heating step. These orientation measurements comprised rocking curves with 20° range with 0.1°/step. Following the alignment and the rocking curve measurements after each annealing step, the near-field camera was removed and the image was magnified by an X-ray objective lens comprised of 88 Be parabolic lenslets (2D focusing optics), each with a R=50 μm radii of curvature. The entry plane of the imaging CRL was positioned $281\,\mathrm{mm}$ from the sample along the diffracted beam, and aligned to the beam using a far-field detector. The objective projected a magnified image of the diffracting sample onto the far-field detector, with an X-ray magnification of $M_\mathrm{x} = 17.9\times$. The far-field imaging detector used an indirect X-ray detection scheme. It was comprised of a scintillator crystal, a visible microscope and a 2160×2560 pixel PCO.edge sCMOS camera. It was positioned $5010\,\mathrm{mm}$ from the sample.

The sample mosaicity was acquired by measuring distortions along the two orthogonal tilts ϕ and χ, cf. figure 1. For the deformed grain and its surroundings the two sample tilt angular ranges were $\Delta\phi = 8^\circ$ and $\Delta\chi = 3^\circ$, respectively. After 240 s of annealing we focused on the RX GOI, and measured it in more detail where the χ-range and step size was $\Delta\phi = 0.3^\circ$ and $\Delta\chi = 0.4^\circ$, respectively. With this data, each voxel can be associated with a subset of a (110) pole figure, allowing us to generate Center of Mass (COM) maps to describe the average direction of the (110) orientation for each voxel in the layer [19].

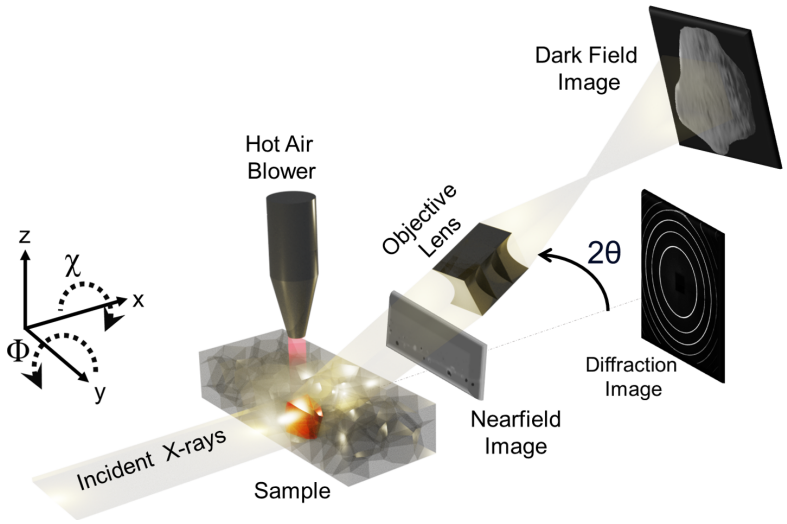

Figure 1. Schematics of DFXM and SXRD setup. A diffracting grain of interest is shown red. DFXM orientation maps comprises two tilts (ϕ and χ) at the constant 2θ angle, and reveal the spatial variation of the orientation of the lattice around the 110 scattering vector.

2.3. Samples and Sample Environments

We studied laboratory produced Fe-3%Si binary cast samples that were hot rolled and annealed having an average grain size of 150 μm before cold rolling [20]. These samples were then cold rolled at a true strain of about $\epsilon_{vm} = 2$, corresponding to 85% reduction in size. The samples remain ferritic due to the high Si content of the alloy. Details of sample preparation is given elsewhere [17, 20]. Different samples from the same batch were used for the EBSD and synchrotron experiments. A hot air blower positioned 5 mm from the sample was used to perform the isothermal annealing steps for the synchrotron annealing studies. A total of 475 s of isothermal heating at $\approx$ 610 °C was applied in 9 intermittent steps, achieving a global recrystallization amount of $\approx$65% [21]. All DFXM measurements were then done at room temperature after air cooling.

3. Microstructure of the Deformed State

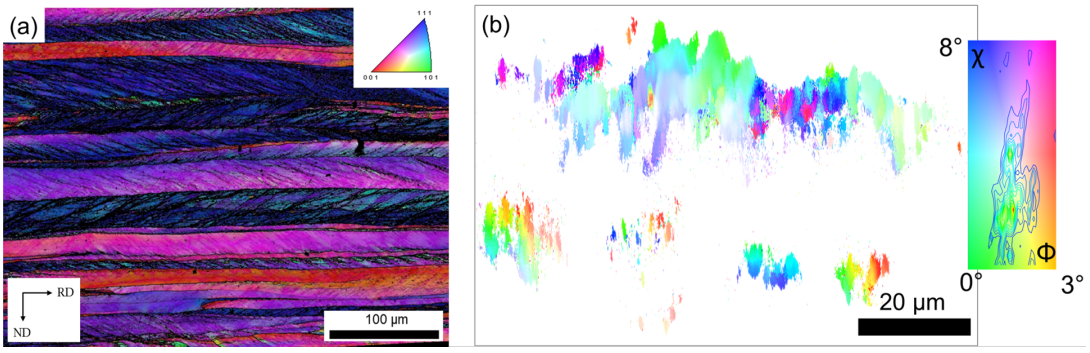

Figure 2. (a) EBSD map of the as-deformed sample. (b) DFXM mosaicity map from a HSE region. Colormap shows the angular spread in the two sample tilts. Note that parts that remain empty in the map because the diffracted intensity from the zones with different orientations isfiltered by the objective.

We begin by presenting the features of the deformed microstructure. Figure 2(a) shows the EBSD mapping of the deformed state displaying a strongly-textured microstructure with heterogeneous

stored energy/dislocation density. Deformation features such as transition bands, shear bands, and deformation bands are present. The deformed microstructure had a typical bcc rolling texture manifested by the marked appearance of α-fibre ($\{hkl\}\langle 110\rangle$), blue-red-magenta colored regions and γ-fibre ($\{111\}\langle uvw\rangle$), blue regions in ND-IPF (Normal Direction Inverse Pole Figure) [22]. It is known that in bcc metals the regions with the highest Taylor factor such as $\{111\}\langle uvw\rangle$ have high stored energy (HSE) [23]. Thus, during the early stages of annealing, these HSE regions typically produce the first RX grains [24–26]. Therefore, we focused on these HSE regions and mapped the 3D orientation of one using DFXM.

Figure 2(b) shows a DFXM mosaicity map of two deformed grains elongated along the rolling direction from HSE regions.The orientation gradients along the rolling direction separate zones with different substructure. The high spatial and angular resolutions afforded by DFXM unveil the fine details of the deformed microstructure located in the HSE regions within the bulk, including cells $<1\ \mu$m having $<8^\circ$ misorientation across the stretched grain. The overall angular spread of the measured deformed grains exceeds 10°. We focus on this deformed grain and follow it through different heating steps.

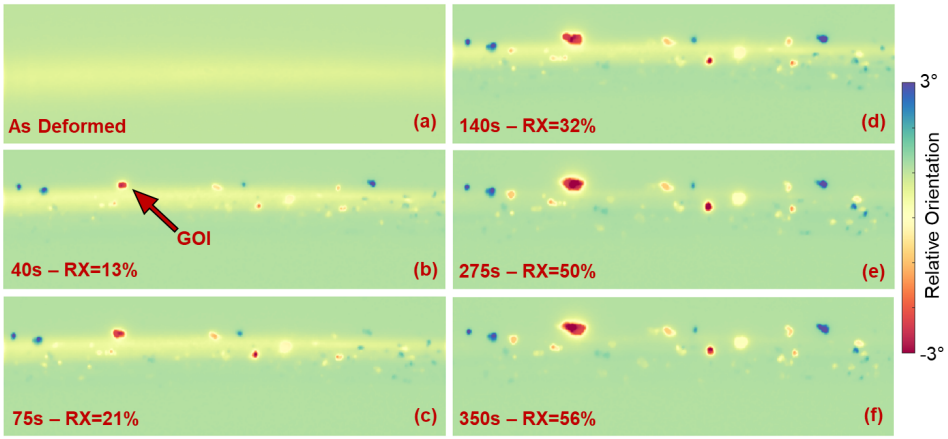

Figure 3. Nearfield rocking curve COM maps at different recrystallization levels. In these images, the nearfield detector shows a section of the Debye–Scherrer 110 ring, $\Delta 2\theta = 0.37^\circ$ (vertical) and $\Delta\chi = 3.13^\circ$ azimuth (horizontal).

To map the local orientation relations between the RX grains and the deformed parent grain before zooming in using DFXM, we measured extended rocking curves with the nearfield camera. By doing so, we can focus on a part of the diffraction ring with high resolution. Figure 3(a) shows generated COM map of the rocking curve measurements of the diffraction pattern from the grain shown in figure 2(b). The deformed grain manifests itself like a "powder diffraction pattern" (with no individually identifiable diffraction spots) on the nearfield camera due to the high angular spread and small cell size on the order of the resolution of the detector. Upon isothermal annealing, (b-f) we observe new recrystallized grains appearing within 10° orientation spread. At the same time, the intensity of the deformed grain (powder diffraction-like) decreases as recrystallization advances. At 350 s of annealing, most of the diffraction signal from the deformed grain is no longer visible, showing that it was consumed by the new RX grains. We focus on a RX grain (designated by the red arrow in figure 3(b)) and measure its 3D structure using DFXM. By looking at the diffraction spot of the RX GOI in the nearfield, we can see that the grain continued to grow up to 140 s, while some small grains in the diffraction ring disappear. The GOI seem to remain almost at the same size and intensity between 275 s and 350 s (figure 3(e-f)).

Now we zoom in on the diffraction ring using DFXM, and look at real space images of the deformed and recrystallized grains. Figure 4 shows the DFXM integrated intensity maps of orientation scans as a function of annealing time and depth in the sample. Note that these scans covered $8^\circ \times 7^\circ$ in ϕ and χ. Each image is a 2D slice of the sample from its bulk. At the as-deformed state (RX=0%) we see that the

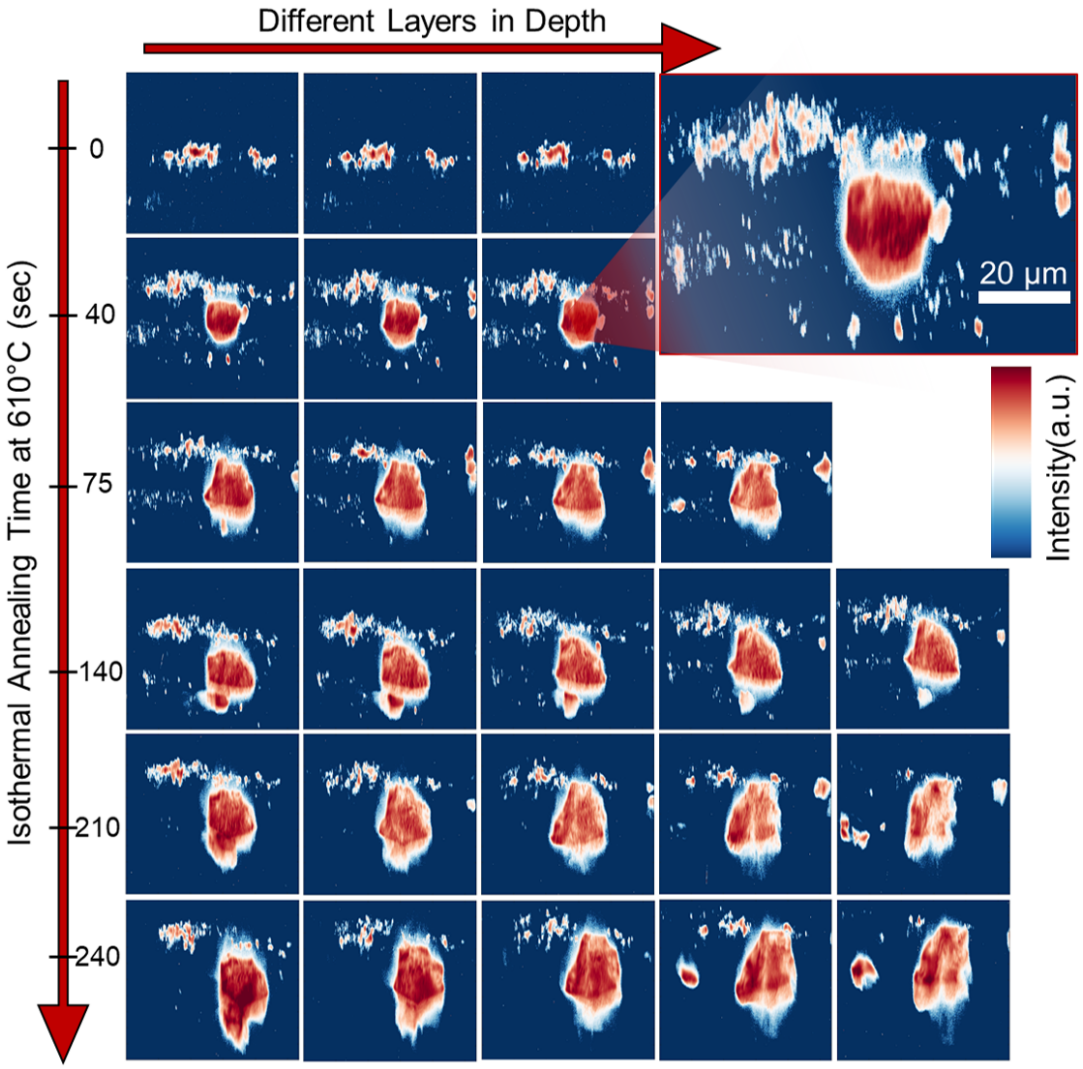

Figure 4. Integrated intensity maps from the DFXM mosaicity scans showing an overview of the annealing microstructures at different positions in the volume and annealing times. Note that the intensity scale is a logarithmic plot.

3D structure of the deformed grain is heterogeneous: different cells with varying diffracted intensities are observed. After 40 s of annealing, we observe some subgrain refinement [27] in the deformed elongated grain, while a substantially larger grain (our GOI shown in figure 3) appears from the empty part of the DFXM image (see the magnified image). This means the GOI seeded from a differently orientated deformed grain, which did not appear in the DFXM image since the CRL objective filtered it out. Moreover, this indicates the region from which the GOI recrystallized, must have a higher stored energy, because it was able to grow faster than any other grain in the field of view. At 40 s, the magnified image of a given layer shows a neighboring grain on the right side of the GOI, which appears to be on the larger side of the other RX grains in the field of view. This indicates that the parent deformed grains for both these grains had the same deformed/RX orientation relations. Upon further annealing the main deformed grain and the refined subgrains continue to vanish at the expense of the RX grains. At 240 s, we observe that all the neighbors of the RX GOI are consumed, and the deformed grain has significantly shrunk.

From 240 s on, we focused on the RX GOI and scanned its orientation in 3D with finer angular steps through the later stages of annealing. Figure 5(a) and (b) show the 3D reconstruction of the GOI with

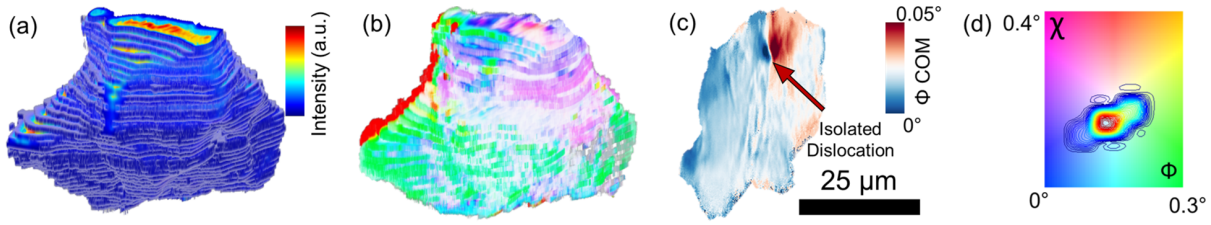

Figure 5. DFXM 3D reconstruction of the GOI at 240 s of annealing (a) using integrated intensity maps (b) using mosaicity maps (c) rocking curve COM map of a selected layer, highlighting an isolated dislocation in bulk (d) orientation color key for the mid layer of the 3D mosaicity scans.

$42 \times 120 \times 1000\,\mathrm{nm}^3$/voxel in x, y, z. Figure 5(a) shows the integrated intensity map while (b) shows the 2D mosaicity map. Figure 5(d) gives the colorkey and the angular spread in the mosaicity map. The GOI shows orientation variations less than 0.3°. Especially the top part of the grain shows more of a heterogeneity compared to the mid layers. This may be a result of the shear strain accommodation from the parent grain at the early stages of nucleation. However, one should be able to observe the onset of nucleation to verify this statement. Figure 5(c) shows the ϕ COM map of a selected layer from the volume of the GOI. For this layer, the angular spread is less than 0.1°. Moreover, we observe isolated dislocations coming out of the plane (almost parallel to the z direction). This dislocation shows a typical positive-negative displacement field around the rotation axis (blue-red colors) [28]. Investigating the layers around this layer, we find that the isolated dislocation marked with the red arrow in figure 5(c) extends $\approx 11\mu$m in the volume. Recently, we showed that in annealed single crystals, isolated dislocations can extend tens of micrometers, while the dislocation boundaries can be on the order of hundreds of micrometers [29]. We observe similar isolated dislocations through the volume of the GOI, which gives us $\approx 0.5-1\times10^{11}\mathrm{m}^{-2}$, inline with the literature [30]. Note that in this study, we probed only one diffraction vector using the DFXM method. Therefore, other dislocations with different orientations may not appear due to their Burgers' vector alignment with respect to the diffraction vector. This signifies that the measured dislocation density must be slightly higher in reality.

Next, we monitor the microstructural evolution of the ROI upon furhter annealing from 240 s to 475 s. figure 6 shows the evolution of the ROI through different stages of isothermal annealing. From 240 s (RX=46%) to 475 s (RX=65%). The integrated intensity maps of the same layer at the thickness shows that the size of the GOI remains the same, meaning that the grain stopped growing after 240 s.

There may be a number of reasons why a grain retains its size during annealing. One possible reason is that the stored energy in the surrounding area is consumed, by the GOI and other recrystallized grains, and therefore the grain requires more energy to grow further. This can result in slower growth or even inhibition of grain growth, which can lead to the recrystallized grain retaining its size during annealing. Another possible reason of similar nature is that the GOI has found a microstructural obstacle e.g. a prior grain boundary or impingement with other recrystallized grains has occured, scenarios which would hinder growth. By inspecting our DFXM data, we unfortunately do not see any other grain neighbouring our GOI, except the one that was consumed between 40-75s of annealing (figure 4), implying that a hypothetical neighboring grain would have a significantly different orientation. This highlights the importance of the neighboring grain information, and shows that the coupling DFXM with coarser grain methods such as 3DXRD and DCT is crucial. It is important to note that the retention of grain size during annealing depends on a variety of factors, including the temperature, time, and strain history of the material. Step-wise isothermal heating like we performed in this experiment may result in slower growth after the early stages of recrystallization because the stored energy can be used for recovery and recrystallization simultaneously more than once. Here we observe a single grain that grew faster than any other grain in the field of view, and retained its size after RX=46% overall.

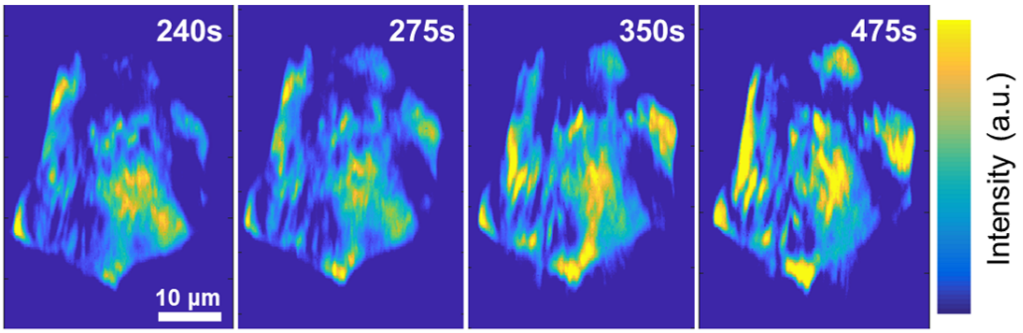

Figure 6. Integrated intensity map of the same 2D layer the ROI through different annealing steps at 610°C.

4. Conclusions and Outlook

We presented a multi-scale investigation of the microstructure and texture evolution of a heavily deformed (85%) ferritic alloy upon isothermal annealing, using a combination of DFXM, SXRD and EBSD methods. For the first time, we show isolated dislocations within a recrystallized ferrite grain in bulk. Our results show the importance of coupling coarser grain methods such as 3DXRD/DCT with DFXM to have a complete multiscale picture of the intragranular (DFXM) and neighbouring grain (3DXRD) information. Combining these methods would yield a powerful "ultra microscope" that can resolve subgrain dynamics and along with texture information, from the deformed to annealing states, offering a whole new perspective in the study of recrystallization.

Acknowledgments

The authors acknowledge the ESRF for provision of beamtime at ID06-HXM. N.M. acknowledges the financial support of the National Association of Research and Technology (ANRT – Project no.1073–2015). HFP acknowledges support from ERC Advanced Grant nr 885022 and from the Danish ESS lighthouse on hard materials in 3D, SOLID.

References

[1] Xu W, Quadir M and Ferry M 2009 *Metallurgical and Materials Transactions A* **40** 1547–56
[2] Zhang Y, Juul Jensen D, Zhang Y, Lin F, Zhang Z and Liu Q 2012 *Scr. Mater.* **67** 320–23
[3] Pantleon W 2008 *Scr. Mater.* **58** 994–97
[4] Konijnenberg P J, Zaefferer S and Raabe D 2015 *Acta Mater.* **99** 402–14
[5] Wright S, Field D and Nowell M 2015 *IOP Conf. Ser.: Mater. Sci. Eng.* vol 89 (IOP Publishing) p 012049
[6] Moussa C, Bernacki M, Besnard R and Bozzolo N 2015 *IOP Conf. Ser.: Mater. Sci. Eng.* vol 89 p 012038
[7] Schmidt S, Nielsen S F, Gundlach C, Margulies L, Huang X and Jensen D J 2004 *Science* **305** 229–32
[8] Hefferan C M e a 2012 *Acta Mater.* **60** 4311–18
[9] Sun J, Yu T, Xu C, Ludwig W and Zhang Y 2018 *Scr. Mater.* **157** 72–75
[10] Xu C, Zhang Y, Godfrey A, Wu G, Liu W, Tischler J Z, Liu Q and Juul Jensen D 2017 *Sci. Rep.* **7** 1–7
[11] Hayashi Y, Hirose Y and Seno Y 2015 *Journal of Applied Crystallography* **48** 1094–101
[12] Simons H *et al.* 2015 *Nat. Commun.* **6** 6098
[13] Poulsen H F, Jakobsen A, Simons H, Ahl S R, Cook P and Detlefs C 2017 *J. Appl. Cryst* **50** 1441–56
[14] Yildirim C, Cook P, Detlefs C, Simons H and Poulsen H F 2020 *MRS Bulletin* **45** 277–82
[15] Gustafson S, Ludwig W, Shade P, Naragani D, Pagan D, Cook P, Yildirim C, Detlefs C and Sangid M D 2020 *Nature communications* **11** 3189
[16] Yildirim C, Mavrikakis N, Cook P, Lamas R R, Poulsen H, Detlefs C and Kutsal M 2022 *IOP Conference Series: Materials Science and Engineering* vol 1249 (IOP Publishing) p 012044
[17] Yildirim C *et al.* 2022 *Scr. Mater.* **214** 114689
[18] Kutsal M 2019 *IOP Conf. Mat. Sci. and Eng.* **580** 012007
[19] Ferrer Garriga J *et al.* 2023 *Journal of Synchrotron Radiation* **30** 527–37
[20] Mavrikakis N e a 2019 *Acta Mater.* **174** 92–104
[21] Mavrikakis N *et al.* 2018 *IOP Conf. Ser.: Mater. Sci. Eng.* vol 375 (IOP Publishing) pp 12–16
[22] Hoelscher M, Raabe D and Luecke K 1991 *Steel Res* **62** 567–75

[23] Dillamore I L and Katoh H 1974 *Metal Science* **8** 73–83
[24] Doherty R D *et al.* 1998 *Materials Today* **1** 14–15
[25] Inagaki H 1994 *ISIJ International* **34** 313–21
[26] Hutchinson W B 1984 *Int. Metals Rev.* **29** 25–42
[27] Jones A, Ralph B and Hansen N 1979 *Proceedings of the Royal Society of London. A. Mathematical and Physical Sciences* **368** 345–57
[28] Caliste T N T, Drouin A, Caliste D, Detlefs C and Baruchel J 2021 *Applied Sciences* **11** 9054
[29] Yildirim C, Poulsen H F, Winther G, Detlefs C, Huang P H and Dresselhaus-Marais L E 2023 *Scientific Reports* **13** 3834
[30] Sui-he J, Wei-min M, Ping Y and Feng Y 2014 *Chinese Journal of Engineering* **36** 1643–49